J. Fluid Mech. (2013), *vol.* 728, *pp.* 279–305. © Cambridge University Press 2013
doi:10.1017/jfm.2013.199

Three-dimensional buoyancy-driven flow along a fractured boundary

Adrian Farcas and Andrew W. Woods†

BP Institute for Multiphase Flow, University of Cambridge, Madingly Road, Cambridge CB3 0EZ, UK

(Received 19 July 2011; revised 3 April 2013; accepted 13 April 2013;
first published online 9 July 2013)

We describe the steady motion of a buoyant fluid migrating through a porous layer along a plane, inclined boundary from a localized well. We first describe the transition from an approximately radially spreading current near the source, to a flow which runs upslope, as it spreads in the cross-slope direction. Using the model, we predict the maximum injection rate for which, near the source, the flow does not fully flood the porous layer. We then account for the presence of a fracture on the boundary through which some of the flow can drain upwards, and calculate how the current is partitioned between the fraction that drains and the remainder which continues running upslope. The fraction that drains increases with the permeability of the fracture and also with the distance from the source, as the flow slows and has more time to drain. We introduce new scalings and some asymptotic solutions to describe both the flow near the fracture and the three-dimensional surface of the injected fluid as it spreads upslope. We extend the model to the case of multiple fractures, so that the current eventually drains away as it flows over successive fractures. We calculate the shape of the region that is invaded by the buoyant fluid and we show that this flow, draining through a series of discrete fractures, may be approximated by a flow that continuously drains through its upper boundary. The effective small uniform permeability of this upper boundary is given by $k_b \approx \int k_f \,\mathrm{d}x/D_F$, where $\int k_f \,\mathrm{d}x$ is the integral of permeability across the width of the fracture and D_F is the inter-fracture spacing. Finally, we discuss the relevance of the work for CO_2 sequestration and we compare some simple predictions of the plume shape, volume and volume flux derived from our model with data from the Sleipner project, Norway for the plume of CO_2 which developed in Horizon 1.

Key words: geophysical and geological flows, gravity currents, low-Reynolds-number flows

1. Introduction

The motion of a buoyant fluid injected into permeable rock has attracted considerable attention in the context of CO_2 sequestration into sub-surface aquifers (e.g. Nordbotten & Celia 2006; Hesse, Orr & Tchelepi 2008), with important issues including the storage capacity of a reservoir and the potential leakage pathways of the CO_2 from the system. Numerous numerical models describing the motion of CO_2 gravity currents have been developed and have led to a series of fascinating results

† Email address for correspondence: andy@bpi.cam.ac.uk

https://doi.org/10.1017/jfm.2013.199 Published online by Cambridge University Press

concerning the subsurface dispersal of a buoyant fluid of low viscosity displacing a second fluid (Pruess *et al.* 2003; Obi & Blunt 2006; Juanes *et al.* 2006; de Loubens & Ramakrishnan 2011). These numerical solutions include a wide range of physical processes. As a complement to these numerical studies, a number of simplified analytical models have been developed, using various asymptotic and similarity techniques, to uncover some of the controlling features of these flows, albeit in a simplified context.

Important contributions include the work of Nordbotten & Celia (2006) who described gravity-driven motion of a buoyant fluid from a central source into a confined horizontal aquifer; they showed that near the source, the whole porous layer is flooded, while further from the source, the current forms a gravity tongue which only partially fills the domain. Lyle *et al.* (2005) presented an analysis of gravity-driven flow in an unbounded aquifer, spreading on a horizontal boundary, in which case the model predicts that the flow depth becomes unbounded near the source. Neufeld *et al.* (2011) and Vella *et al.* (2011) examined the leakage of such a gravity-driven flow through a point and line sink, respectively; their models illustrated that all the flow eventually drains through the sink. Vella & Huppert (2006) extended the analysis to the case of an inclined layer, adopting an approach similar to Lister (1992) to model the transient flow, which demonstrated that far from the source the flow asymptotes to a steady gravity-driven flow in which the cross-slope spreading is controlled by the upslope migration speed (cf. Woods 1999).

As well as these models of flow from a vertical well, there have been a series of models developed for flow from a horizontal line-well. Hesse, Tchelepi & Orr (2006) focused on the motion of a two-dimensional current in an inclined system of finite thickness, and described the transition from an early-time regime in which the current fills the depth of the aquifer, to the late-time regime in which the flow spreads along the upper boundary as a thin current. Pritchard, Hogg & Woods (2001) and Woods & Farcas (2009) examined the impact of drainage through the upper boundary on the upslope propagation distance of such two-dimensional currents and Farcas & Woods (2009) examined how, after injection has ceased, the flow partitions into a component which is capillary trapped in the injected layer and a component which drains into the overlying permeable strata. Many of these papers have adopted an approximate description in which the cross-flow pressure gradients are assumed to be hydrostatic, based on the assumption that the current is long and thin; recently, de Loubens & Ramakrishnan (2011) have presented a detailed asymptotic analysis of the underlying governing equations, identifying conditions under which different approximations are appropriate.

In this contribution, we build on these previous analytical models to explore the motion of a steady three-dimensional gravity current below the upper inclined and fractured boundary of a permeable aquifer, of finite thickness. We consider the case of relatively slow injection so that the flow adjusts from a steady, approximately radially spreading gravity current near the injection well to a shallow upslope-propagating gravity current in the far field, and we determine an expression for the critical flow rate above which the flow floods the whole depth of the aquifer near the source. We then explore the draining of part of the current under gravity through a localized fracture, located a distance L_F from the source. We show that in contrast to the case of a horizontal boundary in which all the injected fluid eventually drains through the fracture (Neufeld *et al.* 2011; Vella *et al.* 2011), with an inclined boundary some of the buoyant fluid may continue running upslope beyond the fracture driven by the along-slope component of gravity. We extend the analysis to account for

https://doi.org/10.1017/jfm.2013.199 Published online by Cambridge University Press

drainage through multiple fractures, and explore the limit in which the model becomes equivalent to the case of a current flowing below a uniform low-permeability barrier. The model leads to predictions of the shape and extent of the zone flooded by the buoyant fluid as it drains through the upper boundary of the formation.

At the outset, we note that in applying such simplified buoyancy flow models to a two-phase flow, such as CO_2–water systems, our objective is to gain insight and understanding about some of the controls on the flow in an idealized limiting situation. If the model of a steady buoyancy-driven flow is applied to a CO_2 plume, there is an implicit assumption that the plume migrates through a layer of uniform saturation with a uniform effective relative permeability, and that the capillary transition zone at the base of the current is thin relative to the depth of the flow. These approximations apply in the limit in which the capillary pressure is small; the transition zone thickness h scales with the ratio of the buoyancy force, $\Delta\rho g$, and the capillary pressure, which in turn is related to the CO_2–water interfacial tension, γ, and the pore scale, δ, leading to the balance $h \sim \gamma/\Delta\rho g\delta$ giving values of order 0.01–0.1 m for the CO_2–water system with pores of size 0.1–1 mm (cf. Bennion & Bachu 2006; Golding *et al.* 2011). This corresponds to a Bond number of order 0.01 based on the pore scale. We also note an estimate for the capillary number Ca for the flow, which balances the viscous stresses with the capillary pressure, and scales as $\mu v\delta^2/\gamma k$ (cf. Lovoll *et al.* 2005), where k is the permeability, μ the dynamic viscosity and v the typical interstitial speed; Ca has values of order 0.1–10 for interstitial speeds of 10^{-5} m s^{-1}, in rock of permeability 10^{-13}–10^{-14} m^2. In applying the model to CO_2, we neglect the possible effects of viscous fingering near the well (cf. Homsy 1987), by assuming that in steady state, the dominant mode of flow is through the most unstable gravitationally-driven finger (cf. Verdon & Woods 2007). We also neglect effects of the dissolution of CO_2 into the underlying water (Riaz *et al.* 2006). Although this may cause a fraction of the flow to change phase, it relies on the presence of undersaturated aquifer water below the plume; however, owing to the relatively long time to replenish this water once it is saturated, any such dissolution is likely to be slow (cf. Woods & Espie 2012).

Although noting these limitations of simplified models, they do provide some of the important building blocks for gaining insight and helping with the interpretation of buoyancy-driven flows in nature and in particular plumes of CO_2. For example, some of the most detailed measurements of the spreading of CO_2 plumes in the sub-surface have been obtained from seismic data at the Sleipner field in the Norwegian North Sea. These suggest that the CO_2 spreads laterally within a series of layers of finite thickness, leaking upwards through the cap rock separating each of the layers, with buoyancy forces playing a key role in the dynamics (Bickle *et al.* 2007; Boait *et al.* 2012). The pattern of spreading appears to be asymmetric, and, noting the challenges relating to the uniqueness in inverting an incomplete data set, one possible interpretation is that the layers are inclined to the horizontal, and so there is a buoyancy force both parallel and normal to the boundary. Our buoyancy-driven flow models are relevant, in steady state, in the case that the injection rate relative to the buoyancy flow speed is sufficiently small that the injected fluid does not flood the whole depth of the layer. For such flow rates, we can follow the evolution from a near-well symmetric spreading of the flow to the upslope laterally spreading motion of the plume once the flow becomes long and thin (cf. Woods 1999). In this limit, we are able to explore the effect of fractures or localized openings in the overlying seal rock which allow a fraction of the flow to drain, and may ultimately limit the lateral extent of the flow.

https://doi.org/10.1017/jfm.2013.199 Published online by Cambridge University Press

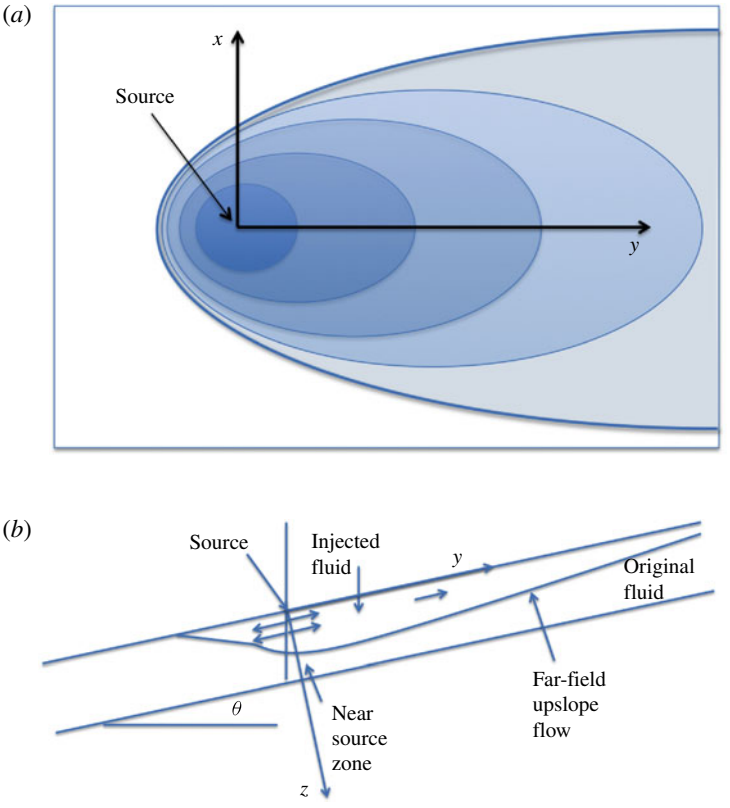


FIGURE 1. (Colour online) Schematic diagram of a generic inclined formation: (*a*) top view, (*b*) side view of adjusting flow. The three-dimensional current of buoyant fluid runs upslope through the main layer of the flow.

2. Governing equations

We assume there is a flux of buoyant fluid issuing from an effective circular source of radius r_s, into an inclined permeable formation of thickness H, permeability k and porosity ϕ with angle θ to the horizontal (figure 1). The buoyant fluid of density ρ_g will then propagate through the porous medium saturated with liquid of density ρ_w, spreading both laterally and along the inclined layer. If the layers are horizontal, and there is no loss of fluid through the boundaries of the layer then, as shown by Nordbotten & Celia (2006), the radius of the zone fully flooded with injected fluid spreads outwards at a rate proportional to $t^{1/2}$, and the original fluid in the system continues to be displaced radially. Depending on the injection rate, this may lead to instability and mixing at the flow front (cf. Homsy 1987; Yortsos & Hickernell 1989). However, in the case that the aquifer has a shallow inclination to the horizontal, then once the flow has spread sufficiently far from the source, we expect that it will adjust to a steadily propagating gravity current running upslope (Woods 1999), with no further displacement of the ambient fluid. In this case, we expect that the flow near the source also converges to a steady state which supplies the far-field steady-state current.

In such gravity-driven flow, provided the supply flux is sufficiently small, the current will become relatively long and thin so that the velocity is, to leading order, parallel

https://doi.org/10.1017/jfm.2013.199 Published online by Cambridge University Press

to the boundary (Barenblatt 1996; de Loubens & Ramakrishnan 2011) and, in the limit in which we neglect capillary effects, to leading order, the pressure gradient in the current in the direction normal to the boundary becomes hydrostatic (cf. Barenblatt 1996; Huppert & Woods 1995; de Loubens & Ramakrishnan 2011). Once the injected fluid has established a steady flow, the original fluid in the aquifer is stationary and therefore has a hydrostatic gradient in the direction both normal to and along the boundary, and this determines the dynamic pressure gradient in the buoyant current. In a Cartesian coordinate system with origin at the centre of the mass source, and aligned with the slope of the inclined layer, of magnitude θ, the pressure in the direction normal to the boundary is expressed as

$$P - P_0 = (\rho_w - \rho_g)gh\cos\theta + \rho_g gz\cos\theta - \rho_w gy\sin\theta \tag{2.1}$$

where x is cross-slope, y is upslope and z is normal to the slope, as illustrated in figure 1, and with P_0 constant. The depth of the current, $h(x, y, t)$, is determined by combining mass conservation with Darcy's law and (2.1). Darcy's law then takes the form

$$\boldsymbol{u} = -\frac{k}{\mu}[\nabla P - \rho_g g(0, -\sin\theta, \cos\theta)] \tag{2.2}$$

where k is the effective permeability for the motion of the injected fluid as it moves through the main layer of rock, here taken to be a constant, and μ is the viscosity of the injected fluid (see Nordbotten & Celia 2006; Hesse *et al.* 2007). Combining (2.1) and (2.2) gives the velocity of the gravity current

$$\boldsymbol{u} = -\frac{k\Delta\rho g}{\mu}\left(\cos\theta\frac{\partial h}{\partial x}, -\sin\theta + \cos\theta\frac{\partial h}{\partial y}, 0\right) \tag{2.3}$$

where $\Delta\rho = \rho_w - \rho_g$. At each point in the flow domain, once a steady flow has become established, the flux of fluid $\boldsymbol{F} = \boldsymbol{u}h$ satisfies

$$\nabla\cdot\boldsymbol{F} = \frac{k\Delta\rho g}{\mu}\left[\cos\theta\nabla^2 h^2 - \sin\theta\frac{\partial h}{\partial y}\right] = 0. \tag{2.4}$$

This corresponds to the steady-state form of the governing equation presented by Woods (1999) and Vella & Huppert (2006) and to the more recent formal derivation by de Loubens & Ramakrishnan (2011), their equation (2.58), in the case that the orignal formation fluid is static. The problem is closed by imposing that there is a constant volume flux Q distributed axisymmetrically about the source of radius r_s:

$$\frac{-2\pi k\Delta\rho g\cos\theta}{\mu}rh\frac{\partial h}{\partial r} = Q \quad \text{at } r = r_s \tag{2.5}$$

and that far upslope, $\int_{-\infty}^{\infty} uh(x, y)\sin\theta\,\mathrm{d}x = Q$ and $h \to 0$.

3. Adjustment from radial flow to upslope flow

We first describe the transition from the near-source flow to the laterally spreading flow which runs upslope into the far field. In steady state, the quantity $(Q/u)^{1/2}$, where $u = k\Delta\rho g/\mu$, has the units of length, and if we scale the depth of the current by $(Q/u\cos\theta)^{1/2}$ and the length by $(Q/u\cos\theta\tan^2\theta)^{1/2}$, then (2.4) reduces to the

https://doi.org/10.1017/jfm.2013.199 Published online by Cambridge University Press

dimensionless form

$$\frac{\partial}{\partial \hat{r}}\left(\hat{r}\hat{h}\frac{\partial \hat{h}}{\partial \hat{r}}\right) = \frac{\partial \hat{h}}{\partial \hat{y}} \tag{3.1}$$

where dimensionless properties are shown using the hat notation and where $\hat{r}^2 = \hat{x}^2 + \hat{y}^2$, while the flux condition (2.5) at the source, $r = r_s$, reduces to

$$-2\pi\hat{r}\hat{h}\frac{\partial \hat{h}}{\partial \hat{r}} = 1, \tag{3.2}$$

i.e. the dimensionless flux is 1. The only parameter remaining in the problem is the dimensionless well radius given by $\gamma = r_s(u\cos\theta\tan^2\theta/Q)^{1/2}$ at which (3.1) applies. Typically, in operating conditions where $Q \approx 10^{-3}$ m^3 s^{-1}, $u\cos\theta\tan^2\theta \approx 10^{-6}$–$10^{-5}$ m s^{-1} and $r_s \approx 0.5$ m, then $\gamma \approx 0.01$. With such a small γ, the far-field flow may be independent of the detailed flow pattern near the source, and indeed we expect it to tend to a steady balance between the cross-slope spreading under gravity and the upslope buoyant advection of the flow (Woods 1999)

$$\hat{h}(\hat{x}, \hat{y}) = \frac{6^{1/3}}{4}\frac{1}{\hat{y}^{1/3}}\left(1 - \frac{4}{6^{4/3}}\frac{\hat{x}^2}{\hat{y}^{2/3}}\right). \tag{3.3}$$

In contrast, with small γ, we expect the flow near the well to be dominated by the cross-slope component of gravity which causes the flow to slump in an approximately axisymmetric fashion, with the leading-order motion near the well being axisymmetric.

Provided the flux is not too large, this equation has steady solution, near the well, of the form

$$\hat{h}^2(\hat{r}) = c_0 - \frac{1}{\pi}\ln\hat{r}, \tag{3.4}$$

where c_0 is a constant. However, as the flow spreads from the well, it gradually adjusts and becomes asymmetric, since all the flow from the source migrates upslope. It then gradually adjusts towards the far-field similarity solution (3.3). To visualize this transition in the flow we have solved (3.1) numerically, for several small values of γ. We have employed an extension of the code in Woods & Farcas (2009), namely an implementation of an alternating direction implicit (ADI) generalized Crank–Nicolson method for nonlinear diffusion, to integrate numerically (3.1). The accuracy of the results was checked to be within 1 % by repeating calculations with one-half the space step. We have found that provided $\gamma \ll 1$, then the motion converges to a universal steady solution for $\hat{r} > \gamma$ (see figure 2*a*,*b*). Near the source, the contours of constant depth decrease in height, and although they retain an approximately circular shape, the centre of the contours gradually migrates upslope. This is a reflection of the fact that all the flux issuing from the source gradually migrates upslope. Beyond a radius of about $\hat{r} \approx 0.2$–0.3 (figure 2*a*), the contours of constant depth cease to be approximately circular, and adjust to the shape of the constant depth contours associated with the upslope asymptotic solution (3.3), see figure 2(*b*).

As a measure of the convergence of the flow to the solution far upstream, we have calculated the function $E(\hat{y})$, which is the cross-slope integral $\int|\hat{h}_N - \hat{h}_S|\,\mathrm{d}x$ of the absolute difference in flow depth between the numerical solution $\hat{h} = \hat{h}_N(\hat{x}, \hat{y})$ and the self-similar solution (3.3), $\hat{h} = \hat{h}_S(\hat{x}, \hat{y})$, as a fraction of the cross-slope integral of the depth of the numerical solution $\int \hat{h}_N\,\mathrm{d}x$ (figure 2*c*). It may be seen that $E(\hat{y})$ decreases

https://doi.org/10.1017/jfm.2013.199 Published online by Cambridge University Press

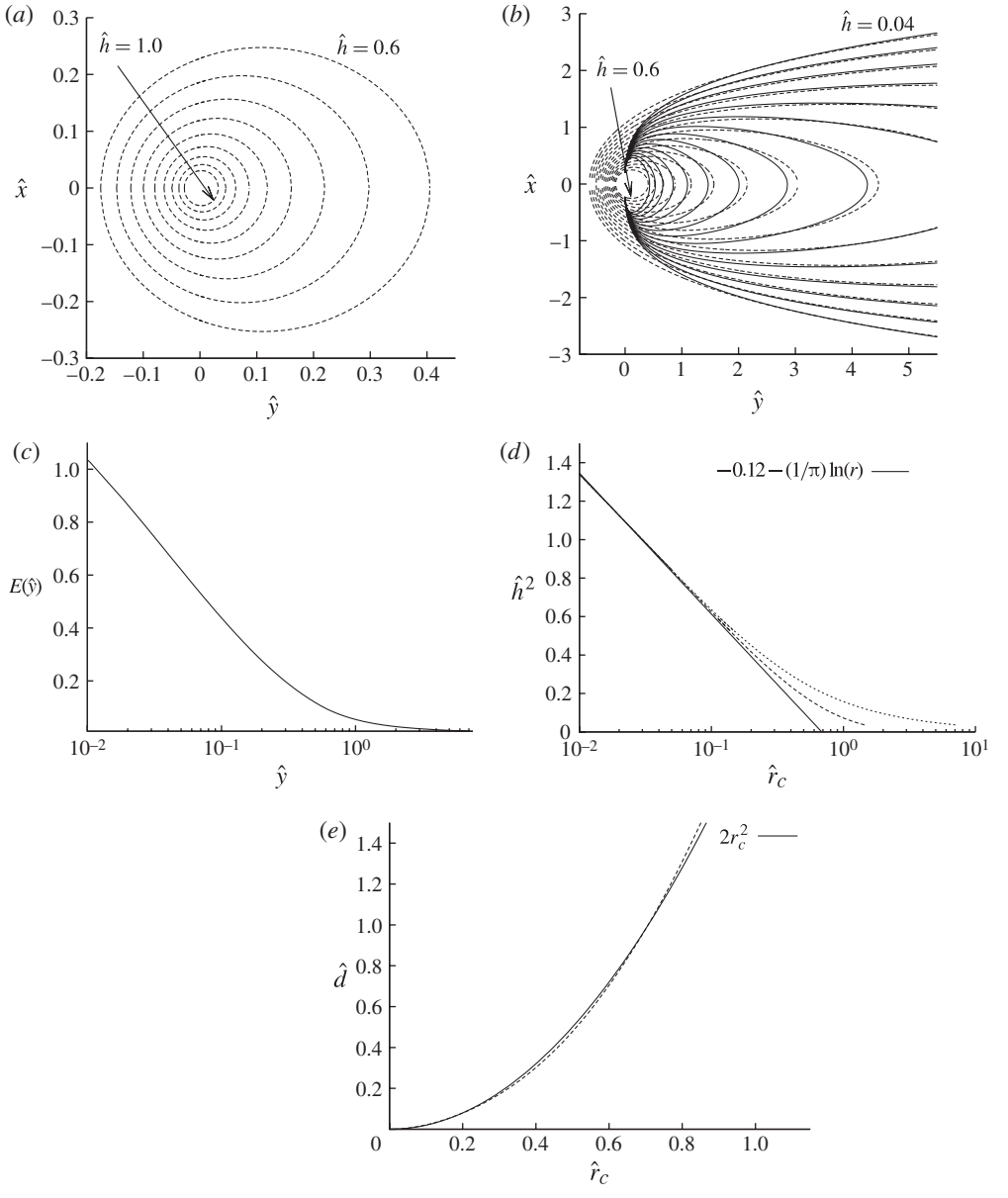


FIGURE 2. (*a*) Near-source and (*b*) far-field numerical (- - -) contours of constant depth, compared with analytical (—) contours of constant depth as given by (3.3). (*c*) Along-slope variation of relative difference $E(\hat{y}) = \int |\hat{h}_N - \hat{h}_S| \, \mathrm{d}x / \int \hat{h}_N \, \mathrm{d}x$ between the numerical solution and the analytical solution (3.3). (*d*) Variation of the square of numerical contour depth with the cross-slope (- - -) and the along-slope ($\cdots$) radius $\hat{r}_c$ of the contours. (*e*) Variation of upslope displacement $\hat{d}$ of contour centre with the cross-slope radius of the contours.

https://doi.org/10.1017/jfm.2013.199 Published online by Cambridge University Press

to 0.05 by the point $\hat{y} = 1.0$, and beyond this point, the solutions have effectively converged (figure 2*c*). We therefore define the adjustment length as

$$L_U = \left(\frac{Q}{u \cos\theta \tan^2\theta} \right)^{1/2}. \tag{3.5}$$

The solution (3.4) for the near-well structure of the flow only applies in the local vicinity of the well, $\hat{r} \ll 1$. However, figure 2(*a*) illustrates that in the region $\hat{r} < 0.4$ the contours of constant depth appear to remain approximately circular, although as the radius increases, the centre of the approximate circle migrates upslope. To explore this further, in figure 2(*d*), we show the variation of the logarithm of one-half the maximum alongslope and cross-slope extent of each contour of constant depth, as a function of the square of the depth of the current. The cross-slope and the along-slope maximum extents are very similar in magnitude, confirming that each contour of constant height is approximately circular, with an approximate radius $\hat{r}_c(h)$. This radius $\hat{r}_c(h)$ appears to follow the functional form of the near-source solution (3.4) (solid line, figure 2*d*), although, as mentioned above, the centre of the contours moves upslope as $\hat{r}_c$ increases (dotted line, figure 2*e*). Indeed, the rate at which the position of the centre of the contours of constant depth, $\hat{d}$, migrates upslope is approximately proportional to the square of the effective radius of the contours of constant depth, $\hat{r}_c$, as shown by the solid line, $\hat{d} = 2\hat{r}_c^2$ in figure 2(*e*). This structure of the near-field solution is valuable for determining the limits of applicability of the model. Indeed, if we constrain the solution in the near-source region to converge to the far-field solution (3.4) which is centred at the well, then we find that the constant c_0 has value $c_0 = -0.12$, and so, in dimensional form, near the well

$$h^2(r_s) = \frac{Q}{u\cos\theta} \left[-0.12 - \frac{1}{\pi} \ln\left(r_s \sqrt{\frac{u\cos\theta\tan^2\theta}{Q}} \right) \right]. \tag{3.6}$$

The above model describes the region of the flow where the depth of the flow is less than the thickness of the aquifer, H. This applies in the case $Q < Q_c$ where Q_c is given implicitly by

$$Q_c \left[\frac{1}{2\pi} \ln Q_c - 0.12 - \frac{1}{\pi} \ln\left(r_s \sqrt{u\cos\theta\tan^2\theta} \right) \right]^{-1} = H^2 u \cos\theta. \tag{3.7}$$

With larger source flux, $Q > Q_c$, the aquifer will be fully flooded for some distance from the source. Subsequently the flow will adjust to the upslope far-field solution. In the remainder of this paper, we focus on the limit $Q < Q_c$ so that the near-source flow is shallower than the depth of the aquifer, and there is no fully flooded region. This limit is relevant for the case of CO_2 sequestration; for example, with a buoyancy flow speed $u = 10^{-5}$ m s^{-1} and $Q = 0.001$ m^3 s^{-1}, then with $\tan\theta = 0.01$ and $r_s = 0.5$ m, the current does not reach the upper boundary provided that $H > 24$ m. The details of the length scale for the transition from near the source to the far field provide a reference for the subsequent calculations in which we allow a fraction of the flow to leak through a fracture in the upper boundary. In particular, the ratio of the transition length to the distance of the fracture from the source is key for interpreting the impact of the fracture on the flow.

https://doi.org/10.1017/jfm.2013.199 Published online by Cambridge University Press

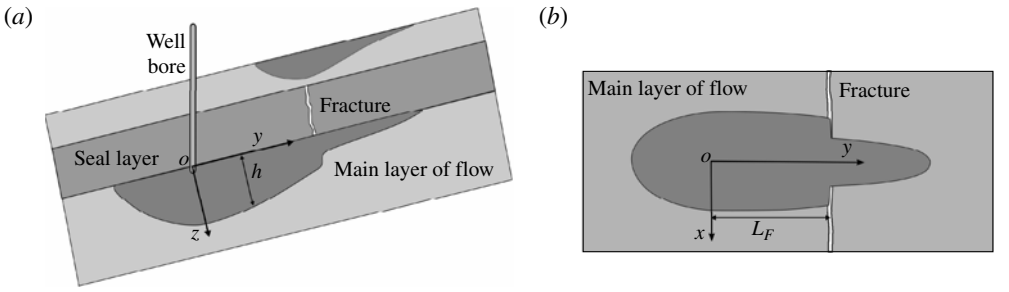


FIGURE 3. Schematic diagram of a generic inclined, fractured formation: (*a*) cross-sectional view, (*b*) top view. The three-dimensional current of buoyant fluid runs upslope through the main layer of the flow and partly drains through a fracture into the overlying layers.

4. Draining into a single fracture

To model draining through the overlying cap rock and for example into a second aquifer, we add a further term to (2.4) to model a sink. The draining may occur through a series of localized fractures or may be more distributed if the cap rock has a small overall permeability. Following Pritchard *et al.* (2001), we model the draining flow as being driven by the local cross-slope hydrostatic head associated with the current. We assume the cap rock has thickness b with local permeability $k_b(x, y) \ll bk/H$ so that the main pressure loss associated with the draining arises in the cap rock, and the assumption of hydrostatic pressure normal to the boundary within the main aquifer still applies (Pritchard *et al.* 2001). Above the cap rock, we assume the pressure is constant relative to hydrostatic, leading to the revised governing equation for steady flow

$$\frac{k\Delta\rho g}{\mu}\left[\cos\theta\nabla^2 h^2 - \sin\theta\frac{\partial h}{\partial y}\right] - \frac{k_b(x,y)\Delta\rho g\cos\theta}{\mu b}h = 0. \tag{4.1}$$

4.1. *Scalings*

Faults and fractures have a complex permeability structure which may vary along fractures and in the damaged zone around the fractures (see for example Evans, Forster & Goddard 1997). For simplicity and convenience, in order to describe the drainage through a fractured zone, we model a cross-slope fracture, located at $y = L_F$, (figure 3) by setting the permeability of the overlying rock to have the form

$$k_b(x, y) = \frac{c_f}{\sqrt{2\pi}\sigma}\exp\left(-\frac{(y - L_F)^2}{2\sigma^2}\right) \tag{4.2}$$

where $c_f = \int_{y=-\infty}^{y=\infty} k_b(x, y)\,\mathrm{d}y$ does not vary in the x-direction, i.e. across slope, and σ is a measure of the width of the fracture. In most cases of relevance $\sigma \ll L_F$, so that the width of the fracture is very small compared to the length scale of the flow, and we do not expect the draining to be very sensitive to the parameter $\beta = \sigma/L_F$ for $\beta \ll 1$. This model for the fracture has been introduced for mathematical convenience, in order to parameterize the finite width of the fracture as well as the strength of the draining, as explained below. We return to this assumption later in this section, when it will be tested numerically. In order to study the flow from the source to the fracture, and the subsequent draining, across the fracture zone, we introduce a new series of scalings for the equations based on the distance to the fracture, L_F. We then use the

https://doi.org/10.1017/jfm.2013.199 Published online by Cambridge University Press

far-field steady solution for the flow (3.3) to provide scalings for the cross-slope width, $W_f = \left(QL_F/u\tan^2\theta\cos\theta\right)^{1/3}$, and depth of the flow, $H_f = \left(Q^2/(u^2\cos^2\theta\tan\theta L_F)\right)^{1/3}$, leading to the dimensionless variables $\hat{x} = x/W_f$, $\hat{y} = h/L_F$ and $\hat{h} = h/H_f$. Equation (2.4) can then be rewritten in dimensionless form

$$\frac{\partial}{\partial\hat{x}}\left(\hat{h}\frac{\partial\hat{h}}{\partial\hat{x}}\right) + \Lambda\frac{\partial}{\partial\hat{y}}\left(\hat{h}\frac{\partial\hat{h}}{\partial\hat{y}}\right) - \frac{\partial\hat{h}}{\partial\hat{y}} - \Omega(\hat{x},\hat{y})\hat{h} = 0 \tag{4.3}$$

where $\Lambda = W_f^2/L_F^2$. After some algebra, one may establish that

$$\Lambda = \left(\frac{L_U}{L_F}\right)^{4/3}. \tag{4.4}$$

Furthermore, the non-dimensional flux is now $\hat{q} = 1$. The drainage parameter function $\Omega(\hat{x},\hat{y})$ is given by

$$\Omega(\hat{x},\hat{y}) = \frac{\omega}{\sqrt{2\pi}\beta}\exp\left(-\frac{(\hat{y}-1)^2}{2\beta^2}\right) \tag{4.5}$$

where the parameter

$$\omega = \frac{c_f}{kb\tan\theta} \tag{4.6}$$

acts like an overall 'strength' of the fracture and $\beta = \sigma/L_F$ represents the width of the fractured draining zone, which we consider to be localized ($\beta \ll 1$). It can be readily observed from (4.5) that given a steady, uniform current of sufficient depth $\hat{h}$, then two fractures having the same 'strength' ω but different 'widths' β_1 and β_2 will drain the same fluid flux per unit length of fracture, namely $\omega\hat{h}$. Furthermore, ~99 % of the draining flux will come from the region $(1 - 3\beta < \hat{y} < 1 + 3\beta)$.

4.2. *Numerical results for draining into a single fracture*

In the limiting case that the fracture is far from the source, $\Lambda \ll 1$, relative to the adjustment length, then with no drainage through the fracture, i.e. $\omega = 0$, the steady shape of the current is given by the far-field solution (3.3). In the case when Λ is not negligible (see (4.3)) and $\omega > 0$, then the shape of the steady current is more complex, and a numerical approach, as described in the previous section, can be used to explore the effects of Λ and fracture parameters.

We have solved numerically (4.3) for various choices of fracture positions L_F, strengths ω, and widths β. Figure 4 presents some typical results for (*a*) $\Lambda = 1$, (*b*) $\Lambda = 10^{-4/3}$ and fractures of strength $\omega = 1$. In these calculations, the width parameter has value $\beta = 0.03$, but very similar results were observed for smaller fracture widths.

It can be seen in figure 4 that the width of the current decreases across the fracture as part of the flow drains through the fracture. However, the remainder of the current continues upslope, in contrast to the case of a horizontal boundary in which case all flow asymptotically drains through the fracture (Neufeld, Vella & Huppert 2009; Neufeld *et al.* 2011; Vella *et al.* 2011). The contours of constant depth predicted by the numerical solution are again shown with dashed lines in figure 4. The contours of constant depth given by the analytical solutions are illustrated with solid lines and are calculated from the non-draining analytical solution (3.3) upstream of the fracture.

https://doi.org/10.1017/jfm.2013.199 Published online by Cambridge University Press

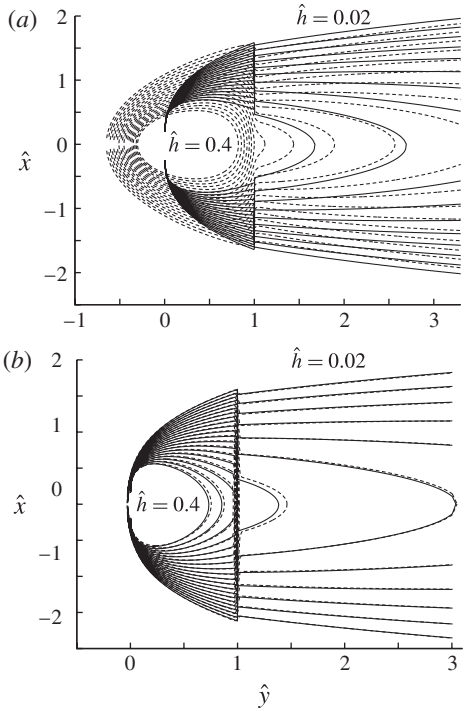


FIGURE 4. Comparison of numerical (- - -) and analytical (—) contours of constant depth ($\hat{h} = 0.02, 0.04, \ldots, 0.4$) for (*a*) $\Lambda = 1$ and (*b*) $\Lambda = 10^{-4/3}$, when draining into a fracture of strength $\omega = 1$.

Downstream of the fracture we employ the solution

$$\hat{h}(\hat{x}, \hat{y}) = \frac{1}{4} 6^{1/3} \frac{A^{2/3}}{(\hat{y} + \hat{y}_s)^{1/3}} \left(1 - \frac{4}{6^{4/3}} \frac{\hat{x}^2}{(A(\hat{y} + \hat{y}_s))^{2/3}}\right),$$
$$\text{for } -\frac{6^{2/3}}{2}(A(\hat{y} + \hat{y}_s))^{1/3} < \hat{x} < \frac{6^{2/3}}{2}(A(\hat{y} + \hat{y}_s A))^{1/3}. \tag{4.7}$$

Here $A = 1 - \hat{q}_D$ is the fraction of the flux which continues to flow beyond the fracture as calculated from the full numerical solutions (see later) and $\hat{y} = -\hat{y}_s$ is the position of the effective source of the current downstream of the fracture, which has been calculated to ensure the continuity of the width of the current at the fracture, $\hat{y} = 1$. The width of the current $2\hat{x}(\hat{y})$ is defined by the relations

$$\hat{h}(\hat{x}(\hat{y}), \hat{y}) = \hat{h}(-\hat{x}(\hat{y}), \hat{y}) = 0. \tag{4.8}$$

Combining this with (3.3) and (4.7) at the fracture $\hat{y} = 1$ leads to the result

$$\hat{y}_s = (1 - A)/A. \tag{4.9}$$

The position of the effective source of the flow downstream of the fracture may be understood in terms of the dependence of the rate of cross-flow spreading of the current with $q^{1/3}$, where q is the flux. Since the flow downstream has a reduced flux, $q(1 - A)$, then in order to spread to the same width as the original current q, it originates further upstream than the actual source.

https://doi.org/10.1017/jfm.2013.199 Published online by Cambridge University Press

It can be observed in figure 4(*b*) that the contours of constant depth predicted by the analytical solution are very close to the numerically calculated contours for the flow both upstream and downstream of the fracture, in the case of slower injection $\Lambda = 10^{-4/3}$. For the faster injection, corresponding to the case $\Lambda = 1$ (figure 4*a*), the analytical solutions still provide a good approximation of the flow, except in the vicinity of the source, where the current adjusts from radial to upslope flow.

4.3. *Local flow and drainage across the fracture*

In order to explore the variation of the steady non-draining flux A with the flow parameters, it is useful to shift the along-slope coordinate by the distance to the fracture L_F, so as to centre it on the fracture, and to rescale it with the width of the fracture σ, i.e. $\tilde{y} = (y - L_F)/\sigma$. We still use W_f and H_f as scales for the width and the depth of the current, i.e. $\tilde{x} = x/W_f$ and $\tilde{h} = h/H_f$, so that the non-dimensional flux upstream of the fracture is still $\tilde{q} = 1$. The draining fraction of the flux $\tilde{q}_D$ is also unchanged by these new scalings, i.e. $\tilde{q}_D = \hat{q}_D = 1 - A$. The steady-state equation describing the flow near the fracture can now be expressed as

$$\beta \frac{\partial}{\partial \tilde{x}} \left(\tilde{h} \frac{\partial \tilde{h}}{\partial \tilde{x}} \right) + \tilde{\Lambda} \frac{\partial}{\partial \tilde{y}} \left(\tilde{h} \frac{\partial \tilde{h}}{\partial \tilde{y}} \right) - \frac{\partial \tilde{h}}{\partial \tilde{y}} = \tilde{\Omega}(\tilde{x}, \tilde{y}) \hat{h}, \tag{4.10}$$

where $\tilde{\Lambda} = W_f^2/\sigma L_F$ can be rewritten as

$$\tilde{\Lambda} = \frac{{L_U}^{4/3}}{\sigma {L_F}^{1/3}} \tag{4.11}$$

and represents a measure of the near-source adjustment distance from radial to upslope flow compared to a combination of the fracture width and the distance from the source.

The drainage function is now given by

$$\tilde{\Omega}(\tilde{x}, \tilde{y}) = \frac{\omega}{\sqrt{2\pi}} \exp\left(-\frac{\tilde{y}^2}{2} \right) \tag{4.12}$$

and therefore depends only on the drainage parameter ω and the along-slope position relative to the mid-line of the fracture.

In this new frame described by (4.10), the draining fraction of the flux depends on three parameters: along-slope diffusion parameter $\tilde{\Lambda}$, the drainage parameter ω, and the fracture width parameter β.

In figure 5 we show the variation of the fraction of the flux $\tilde{q}_D$ which drains through the boundary, as a function of the fracture width parameter β, for a few typical values of $\tilde{\Lambda}$. The drainage parameter was taken as $\omega = 1$ in all cases illustrated in figure 5. As anticipated, it can be seen that in the cases when the fracture is narrow, i.e. $\beta \ll 1$, the drained flux $\tilde{q}_D$ varies very little with fracture width, β, for a fixed total fracture strength, ω. This is because there is little along-fracture flow over the time required for the flow to pass over the fracture. The figure also shows that as $\tilde{\Lambda}$ increases, the cross-slope component of gravity has an increased influence on the flow and acts to reduce the fraction which drains. Large $\tilde{\Lambda}$ corresponds to fractures close to source for which the unscaled current is deeper.

In figure 6 we illustrate the variation of the fraction of the flux $\tilde{q}_D$ which drains through the boundary, as a function of the fracture strength ω, for a series of values

https://doi.org/10.1017/jfm.2013.199 Published online by Cambridge University Press

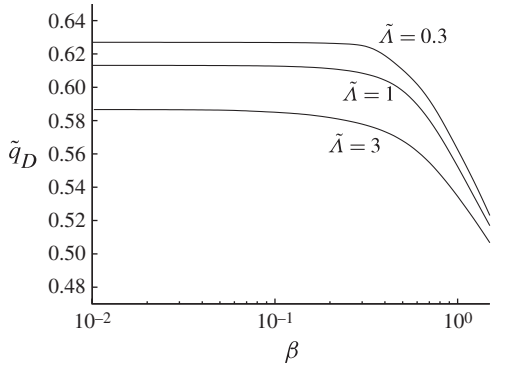


FIGURE 5. Variation of the draining fraction $\hat{q}_D$ with the fracture width parameter β, for $\tilde{\Lambda} = 0.3$, $\tilde{\Lambda} = 1$ and $\tilde{\Lambda} = 3$, where $\tilde{\Lambda}$ is defined in (4.11). The fracture strength is $\omega = 1$.

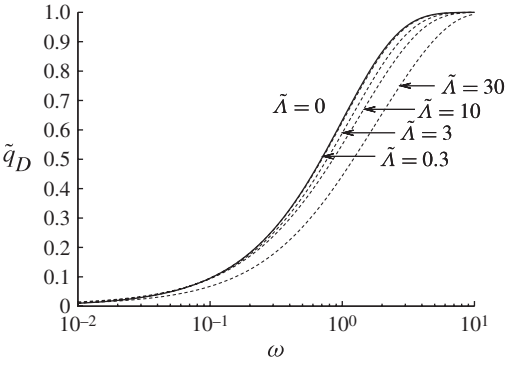


FIGURE 6. Variation of the draining fraction $\hat{q}_D$ with the fracture strength ω for $\tilde{\Lambda} = 30$, $\tilde{\Lambda} = 10$, $\tilde{\Lambda} = 3$ and $\tilde{\Lambda} = 0.3$ (- - -), compared with the analytically calculated variation for the case $\tilde{\Lambda} = 0$ (—).

of the parameter $\tilde{\Lambda}$, according to (4.10). The fracture width parameter was chosen as $\beta = 0.02$ which, according to figure 5, is small enough to ensure that the results of figure 6 would not be substantially different if narrower fractures were considered. For small fracture strengths ω the draining fraction $\tilde{q}_D$ has a linear variation with ω, because the depth of the current is not affected very much as the current passes the fracture. However, with increasing ω, more flux is lost into the fracture until virtually all the current drains. It can be also observed in figure 6 that the draining fraction decreases when parameter $\tilde{\Lambda}$ increases, in accord with figure 5. This is due to the fact that for a current which carries a constant flux $\tilde{q} = 1$, an increase in $\tilde{\Lambda}$ corresponds to an increase in the flow speed across the fracture, leading to a decrease in the height of the current. This decrease in height leads to a decreased draining into the fracture. The maximum draining flux for a given fracture strength ω is obtained in the limit case $\tilde{\Lambda} = 0$. In this limit, the along-slope component of gravity does not cause the current to speed up as a result of the decrease in depth of the flow associated with the draining. In this limit case, for narrow fractures, i.e. $\beta \ll 1$, (4.10) can be

https://doi.org/10.1017/jfm.2013.199 Published online by Cambridge University Press

approximated as

$$\frac{\partial \tilde{h}}{\partial \tilde{y}} = -\Omega(\tilde{x}, \tilde{y})\hat{h}. \tag{4.13}$$

The decrease in height along an arbitrary line across the fracture is $\Delta\tilde{h} = \tilde{h}_0(1 - \exp(-\omega))$ where $\tilde{h}_0$ is the height of the current upstream of the fracture. By integrating this decrease in height along the fracture, the maximum draining flux $\tilde{q}_{max}$ is obtained and has the form

$$\tilde{q}_{max} = 1 - \exp(-\omega). \tag{4.14}$$

The variation of $\tilde{q}_{max}$ with ω is shown with a continuous line in figure 6.

For small $\tilde{\Lambda}$ the draining flux $\tilde{q}_D$ does not differ very much from the analytical solution $\tilde{q}_{max}$, as seen in figure 6 where the plots corresponding to $\tilde{\Lambda} = 0.3$ and $\tilde{\Lambda} = 0$ are almost graphically indistinguishable. It can also be seen in figure 6 that, for a fixed value of the drainage parameter ω, the variation of the draining flux $\tilde{q}_D$ with the parameter $\tilde{\Lambda}$ is less pronounced for $\omega \ll 1$ or $\omega \gg 1$, i.e. for fractures which drain little or almost all of the injected flux.

5. Draining through a pervasively fractured layer

In many situations fractures may be distributed throughout the cap rock as a result of regional stresses acting on the geological formation. This may lead to a series of localized sites at which the current partially drains into the overlying formation. We now adapt the model to investigate the effect of draining through a series of fractures in the cap rock (figure 7), with the objective of characterizing the effective permeability of the cap rock to such leakage. We model a system of multiple fractures, located at $y = \cdots - 2D_F, -D_F, 0, D_F, 2D_F, \ldots$, by setting the permeability of the seal rock to have the form

$$k_b(x, y) = \sum_{i=-\infty}^{i=\infty} k_i(x, y) \tag{5.1}$$

where $k_i(x, y)$ is the permeability associated with the fracture located at $y = iD_F$, which we model in a similar way as in the previous section:

$$k_i(x, y) = \frac{c_f}{\sqrt{2\pi}\sigma} \exp\left(-\frac{(y - iD_F)^2}{2\sigma^2}\right). \tag{5.2}$$

Here $c_f = \int_{y=-\infty}^{y=\infty} k_i(x, y)\,\mathrm{d}y$ is the same for all fractures. Since the fractures are localized, we are interested in the limit $D_F \gg \sigma$ and, as in the case of a single fracture, we expect that the draining does not depend on parameter $\beta = \sigma/D_F$ in the limit $\beta \ll 1$.

In contrast to the single fracture model, the flux continues to decrease with distance upslope as it passes successive fractures and gradually drains. Thus, in developing a model for multiple fractures, it is useful to define a draining length scale. In § 3, we showed that the fraction which drains in a single fracture has the maximum value $1 - \exp(-\omega)$, see (4.14), and so the minimum remaining fraction of the flux after draining in N successive fractures can be approximated as $\exp(-N\omega)$. The minimum number of fractures which reduce the flux to an arbitrarily small value scales as $N_\epsilon \sim O(1/\omega)$ and we choose the draining length scale as the along-slope distance L_D

https://doi.org/10.1017/jfm.2013.199 Published online by Cambridge University Press

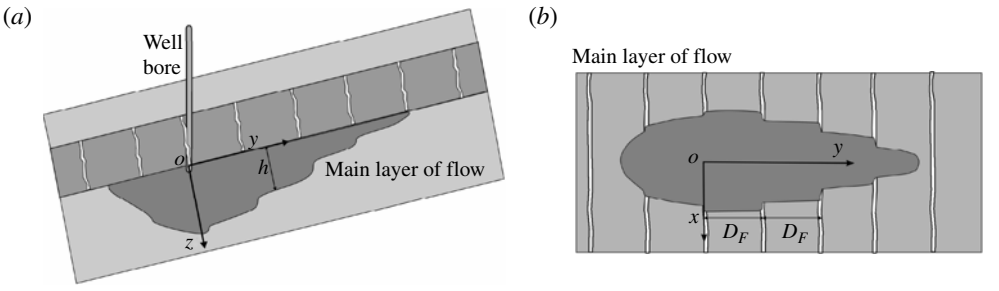


FIGURE 7. Schematic diagram of a generic inclined, fractured formation: (*a*) cross-sectional view, (*b*) top view. The three-dimensional current of buoyant fluid runs upslope through the main layer of the flow and partly drains through a series of fractures into the overlying layers.

covered by these N_ϵ fractures, i.e.

$$L_D = \frac{D_F}{\omega} = \frac{kbD_F \tan\theta}{c_f}. \tag{5.3}$$

Since we are interested in the evolution of the current as the flux decreases to zero through draining, it is appropriate to rescale the along-slope coordinate in terms of L_D and we use a new scale for depth given by

$$H^* = W^{*2} \tan\theta / L_D \tag{5.4}$$

where the continuity of flux in the upslope direction requires that

$$W^* = \left(\frac{L_D q}{u \sin\theta \tan\theta} \right)^{1/3}.$$

If we redefine the non-dimensional variables as $\hat{x} = x/W^*$, $\hat{y} = y/L_D$ and $\hat{h} = h/H^*$, then (2.4) can be rewritten as

$$\frac{\partial}{\partial \hat{x}} \left(\hat{h} \frac{\partial \hat{h}}{\partial \hat{x}} \right) + \Lambda^* \frac{\partial}{\partial \hat{y}} \left(\hat{h} \frac{\partial \hat{h}}{\partial \hat{y}} \right) - \frac{\partial \hat{h}}{\partial \hat{y}} - \Omega^*(\hat{x}, \hat{y}) \hat{h} = 0 \tag{5.5}$$

where $\Lambda^* = W^{*2}/L_D^2$ and the non-dimensional flux is still $\hat{q} = 1$. The drainage parameter function $\Omega^*(\hat{x}, \hat{y})$ is given by

$$\Omega^*(\hat{x}, \hat{y}) = \frac{\omega}{\sqrt{2\pi}\beta} \exp\left(-\frac{(\hat{y}/\omega - i)^2}{2\beta^2} \right). \tag{5.6}$$

Therefore ω is a measure of 'strength' of an individual fracture while $1/\omega = L_D/D_F$ is a scale for the number of individual fractures over which the current spreads upslope while draining.

By observing that $W^{*3} = L_U^2 L_D$, the parameter Λ^* can be rewritten as

$$\Lambda^* = \left(\frac{L_U}{L_D} \right)^{4/3} \tag{5.7}$$

and therefore it depends on the ratio of the adjustment distance L_U from radial to upslope flow to the drainage length L_D.

https://doi.org/10.1017/jfm.2013.199 Published online by Cambridge University Press

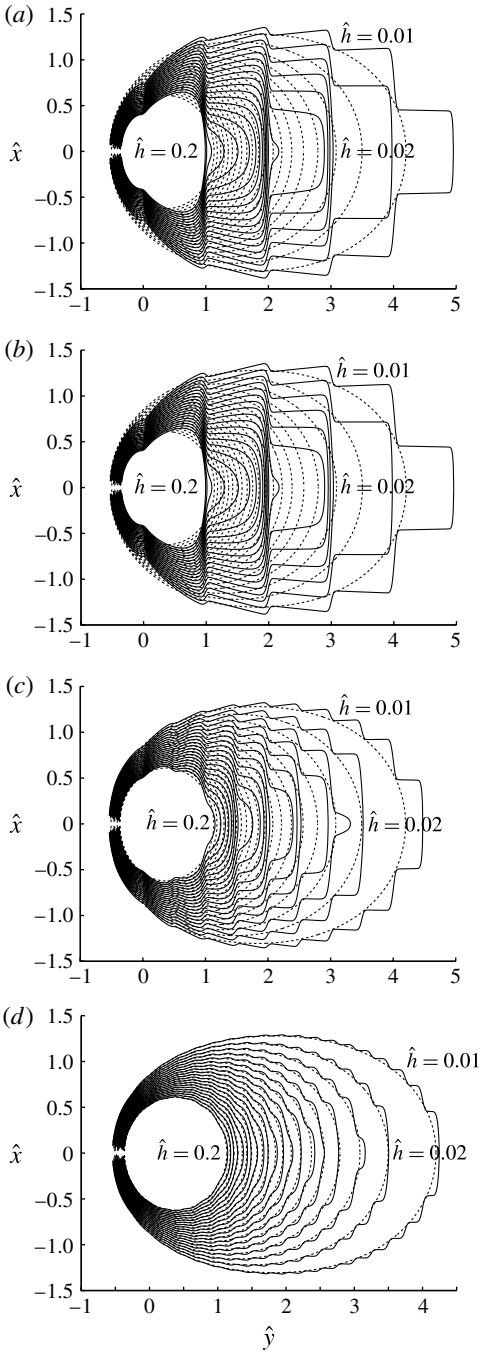


FIGURE 8. Comparison of multi-fracture-draining (—) and uniform-draining (- - -) numerical contours of constant depth ($\hat{h} = 0.01, 0.02, \ldots, 0.2$) for fracture strengths (*a*) $\omega = 1$, (*b*) $\omega = 0.75$, (*c*) $\omega = 0.5$ and (*d*) $\omega = 0.25$, when $\Lambda^* = 1$.

Figure 8 illustrates the contours of constant depth of the steady-state current as it spreads and drains through a multi-fractured formation, as obtained from solving

https://doi.org/10.1017/jfm.2013.199 Published online by Cambridge University Press

(5.5)–(5.6) numerically for various fracture strengths ω. In all cases $\Lambda^* = 1$ and the fracture width parameter was taken $\beta = 0.01$, but very similar results were observed with smaller β, i.e. for narrower fractures. For comparison, we also show in figure 8 the corresponding contours in the case when there is uniform draining through the cap rock, which now has a constant permeability k_b equal to the 'average permeability', i.e.

$$k_b(x, y) = k_b = \frac{c_f}{D_F}. \tag{5.8}$$

In this case, the drainage parameter function Ω^* from (5.5) is constant, namely $\Omega^*(\hat{x}, \hat{y}) = 1$, and the length scale L_D can be expressed as

$$L_D = \frac{kb \tan\theta}{k_b}. \tag{5.9}$$

It can be observed in figure 8 that in all cases the steady-state current spreads along-slope covering a distance of about $5L_D$ by the time the current depth has decreased to $\hat{h} = 0.01$. This confirms that the draining distance indeed scales with L_D, both when the draining is 'uniform' and when it is highly localized near the fractures.

If we interpret the results from figure 8 in unscaled, dimensional units, then we can see that the draining distance is inversely proportional to the fracture strength, for a given interfracture distance D_F. As seen in figures 8(*a*), 8(*c*) and 8(*d*), the current spreads over 5, 10 and 19 fractures when the strength is $\omega = 1$, 0.5 and 0.25, respectively.

It can also be observed from figure 8 that the contours of the uniform-draining numerical solution are close to the corresponding contours of the multi-fracture draining solution, even when current drains through a small number of 'stronger' fractures, as in the case $\omega = 1$. With increasingly weaker fractures, $\omega = 1$, 0.75, 0.5 and 0.25, the uniform-draining solution becomes a progressively better approximation to the multi-fracture solution. In figure 8(*d*), when $\omega = 0.25$, the contours of the uniform-draining solution match very well the multi-fracture solution contours, even if the drainage through the fractures is still very localized, i.e. $\beta \ll 1$. Therefore, we can conclude that the uniform-draining case describes the solution in the limit case of increasingly weak fractures, when $\omega \ll 1$. Next, we focus our attention on the uniform-draining case, and the influence of parameter Λ^* on the solutions of (5.5)–(5.6) in this case.

6. Numerical results for uniform draining

In the limit case of very slow injection and/or drainage (as $\Lambda^* \sim O(Q^{2/3}k_b^{4/3})$) the adjustment distance to upslope flow L_U is negligible when compared with the drainage distance L_D, $\Lambda^* \ll 1$, and the steady shape is given by

$$\frac{\partial \hat{h}}{\partial \hat{y}} = \frac{\partial}{\partial \hat{x}}\left(\hat{h}\frac{\partial \hat{h}}{\partial \hat{x}}\right) - \hat{h}. \tag{6.1}$$

This equation admits the analytical solution (Woods 1999; Vella & Huppert 2006; Woods & Farcas 2009)

$$\hat{h}(\hat{x}, \hat{y}) = \frac{6^{1/3}}{4}\frac{\exp(-\hat{y})}{(1-\exp(-\hat{y}))^{1/3}}\left(1 - \frac{4}{6^{4/3}}\frac{\hat{x}^2}{(1-\exp(-\hat{y}))^{2/3}}\right). \tag{6.2}$$

https://doi.org/10.1017/jfm.2013.199 Published online by Cambridge University Press

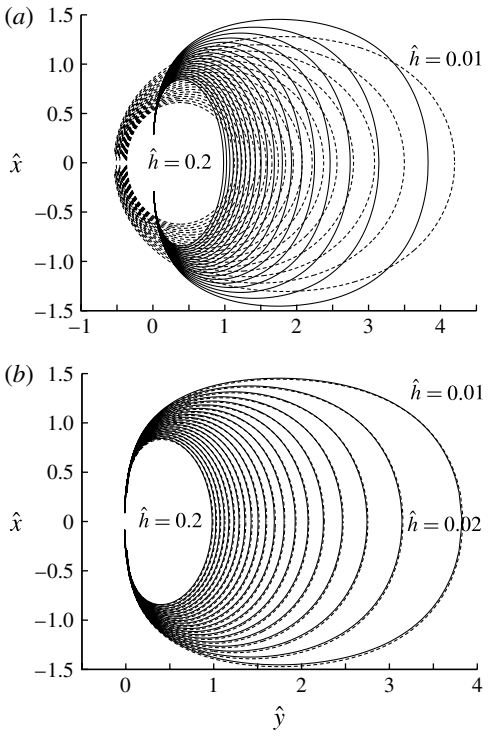


FIGURE 9. Comparison of numerical (- - -) and analytical (—) contours of constant depth ($\hat{h} = 0.01, 0.02, \ldots, 0.2$) for (*a*) $\Lambda^* = 1$ and (*b*) $\Lambda^* = 10^{-2}$.

We compare now the analytical solution (6.2) with the numerical solutions of (5.5) where $\Omega^*(\hat{x}, \hat{y}) = 1$, obtained in the case when Λ^* is non-zero. In figure 9 we show, in rescaled variables, some typical results for the spatial distribution of the contours of constant depth of the steady-state current. This figure illustrates how the current spreads and drains as it migrates upslope along a low-permeability barrier, for figure 9(*a*) $\Lambda^* = 1$ and figure 9(*b*) $\Lambda^* = 0.01$. The numerical contours are displayed with dashed lines and, for comparison, the analytical solution (6.2), which corresponds to the limit case $\Lambda^* \ll 1$, is also shown in figure 9 with continuous lines. It can be seen that for fast injection and/or fast drainage, when the effects of the along-slope diffusion term $\Lambda^*(\hat{h}\hat{h}_{\hat{y}})_{\hat{y}}$ are not negligible, the numerical solution is clearly distinct from the analytical one. The along-slope diffusion causes spreading and drainage upstream, in the region $\hat{y} < 0$, which is not predicted by the analytical solution, and it also causes more spreading than the analytical one-dimensional model in the downstream region $\hat{y} > 0$. In the case of slow injection and/or slow drainage $\Lambda^* = 0.01$, the effects of the along-slope diffusion are negligible compared to the effects of the along-slope convection proportional to $\hat{h}_{\hat{y}}$, and the numerical solution coincides almost exactly with the analytical solution (6.2).

It should be noted that, irrespective of Λ^*, the effect of the along-slope diffusion decreases in the region $\hat{y} \gg 1$. However, for large Λ^* the analytic prediction for the contours of constant depth do not asymptote to the numerical solution for $\hat{y} \gg 1$. This is due to the fact that in the full numerical solutions more flux drains near the source

https://doi.org/10.1017/jfm.2013.199 Published online by Cambridge University Press

(partly in the upstream region), and so less flux is carried downstream than predicted by the one-dimensional analytical model (6.1). This mismatch between the numerical and analytical solution is maintained even as the along-slope diffusion subsides further from the source region. However, this observation suggests that a better agreement between the analytical and numerical solutions could be obtained, at least further away from the source, if the analytical solutions were adjusted to account for the increased draining upslope of the source. This requires a reduction Δq in the effective flux used in the analytical solution and an adjustment of the effective location of the source upslope. We rewrite the analytical solution (6.2) as

$$h(\hat{x},\hat{y}) = \frac{6^{1/3}}{4}\frac{\hat{q}_{an}^{1/3}\exp(-\hat{y}+\Delta y)}{(1-\exp(-\hat{y}+\Delta y))^{1/3}}\left(1-\frac{4}{6^{4/3}}\frac{x^2}{q_{an}^{2/3}(1-\exp(-\hat{y}+\Delta y))^{2/3}}\right) \quad (6.3)$$

where the injected flux used in the analytical solution has the value $\hat{q}_{an} = 1 - \Delta q$ in order that this analytical solution, of type (6.3), matches with the numerical solution far from the source. The source position of this matching analytical solution is also translated downstream by a distance Δy. In the present matching calculations, we have chosen to match the contour lines $\hat{h} = 0.01$ and $\hat{h} = 0.02$, which are the outermost contours shown in figure 9.

Figure 10 illustrates some typical steady-state numerical solutions of the current, shown as a series of contours of constant depth of the flow. These are compared with the matching analytical solution, for decreasing values of the parameter Λ^*. The variation of the flux correction Δq and source displacement Δy with the parameter Λ^* is shown in figure 11.

As expected, smaller corrections are necessary with decreasing Λ^* and they become negligible for $\Lambda^* < 0.01$ (figure 11). However, for larger values of Λ^* there is a good agreement between the numerical and the matched analytical profiles, except in the immediate vicinity of the source, even if large corrections Δq and Δy are needed, as seen in figure 10.

7. Application

As a simple example, to illustrate the possible application of the analysis, we consider the case of CO_2 injection in the Utsira sand reservoir at Sleipner in the North Sea. Here supercritical CO_2 has been injected at a rate of about 1 Mt y^{-1} since 1996 and imaged by time-lapse seismic data starting from 1999, see figure 12.

As described in detail in Chadwick, Arts & Eiken (2005), Bickle *et al.* (2007) and Boait *et al.* (2012), the Utsira formation has nine horizons or main layers of flow separated by mudstones. The CO_2 is injected into the formation from a 38 m section of a horizontal well, which can be approximated as point source as the dimensions of the plume are approximately two orders of magnitude larger. The injection point is located at 1010–1013 m below sea level and its position is indicated in figure 12 with a black dot. Although there is some uncertainty, Chadwick *et al.* (2005) proposed that the main mechanism which brings CO_2 into the flow layers is a 'vertical chimney' structure (visible in the seismic plots, see figure 12). This suggests that the main CO_2 flux is entering layer 1 from the chimney which goes through the layers some 150 m from the well point, and seen as a darker spot in figure 13. The chimney is feeding CO_2 directly from the well into all the flow layers, which would otherwise receive only the CO_2 which drains from the layers underneath.

The flow in Horizon 1 does not receive CO_2 from any layers underneath but from a point source, and also it seems to be close to steady state in the period 1999–2002;

https://doi.org/10.1017/jfm.2013.199 Published online by Cambridge University Press

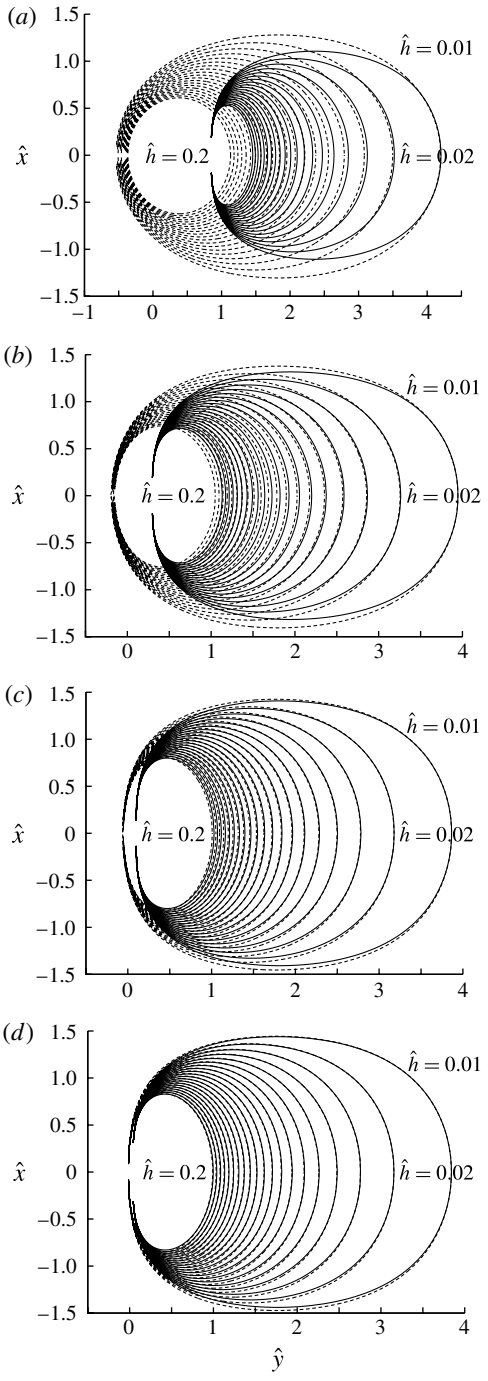


FIGURE 10. Comparison of numerical (- - -) and matched analytical (—) contours of constant depth ($\hat{h} = 0.01, 0.02, \ldots, 0.2$) for (*a*) $\Lambda^* = 1$, (*b*) $\Lambda^* = 10^{-2/3}$, (*c*) $\Lambda^* = 10^{-4/3}$ and (*d*) $\Lambda^* = 10^{-2}$.

https://doi.org/10.1017/jfm.2013.199 Published online by Cambridge University Press

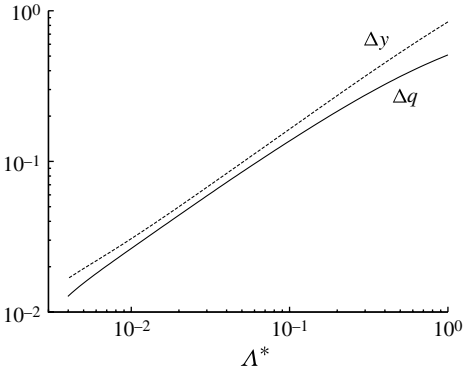


FIGURE 11. The variation of the flux Δq (—) and position Δy (- - -) corrections with the parameter Λ^*.

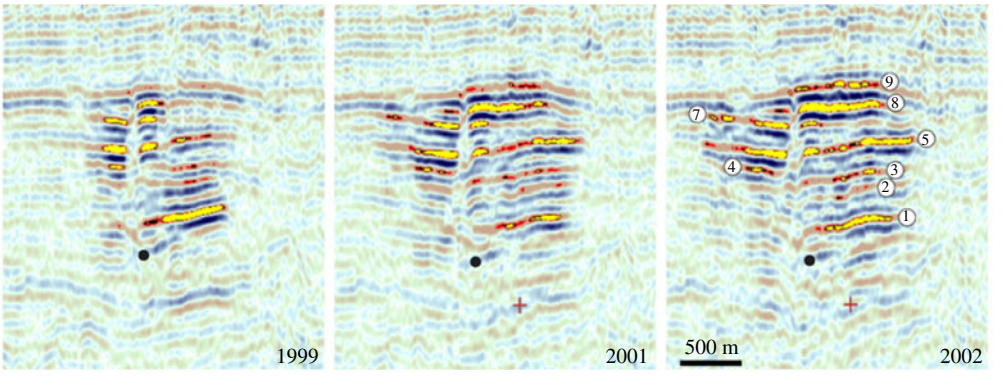


FIGURE 12. (Colour online) Seismic reflection profiles from 1999, 2001 and 2002 surveys at Sleipner. Layers (horizons) are numbered in 2002 profile (after Bickle *et al.* 2007, reused with permission from Elsevier).

although there are numerous possibilities for the nature of this flow (Boait *et al.* 2012) it is nonetheless of interest to examine how we might compare the model developed in this work with the observations, which may be consistent with a picture in which the flow is leaking through the upper seal rock; we stress that owing to the simplicity of the model, this comparison is primarily designed to build insight about the processes. The model we have developed for uniform draining in §§ 5 and 6 may be used to describe flow through a permeable seal rock or flow through a series of fractures in an impermeable seal rock. The model has only one parameter, Λ^*, which incorporates all the flow and reservoir parameters, after scaling. We aim to identify this parameter Λ^* as well as the scaling units, namely the length scale L_D for the distance spread along-slope, W^* for the cross-slope distance, H^* for height of the current, and to see if our model compares with the observational data.

In figure 13, it can be seen that the current in Horizon 1 has spread a distance of about $\mathscr{L} = 1000$ m upslope and $\mathscr{W} = 550$ m cross-slope. It should be noted that the detection limit for CO_2 thicknesses is about ≈ 0.5 m, which is $\sim 10\,\%$ of the typical maximum thickness of the CO_2 plumes (Bickle *et al.* 2007). In figure 14 we

https://doi.org/10.1017/jfm.2013.199 Published online by Cambridge University Press

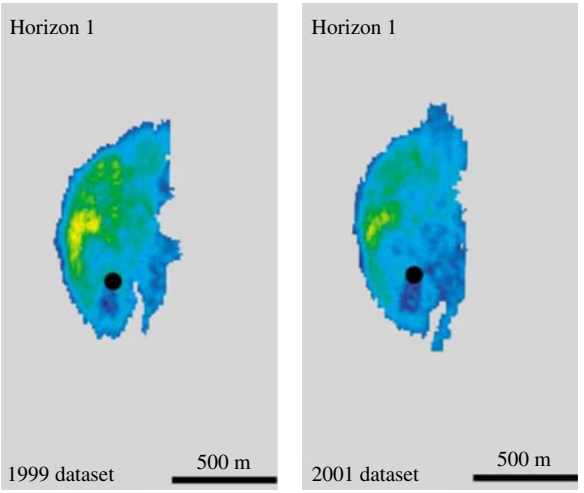


FIGURE 13. (Colour online) Horizon 1 at Sleipner from the 1999 and 2001 seismic survey (after Chadwick *et al.* 2005).

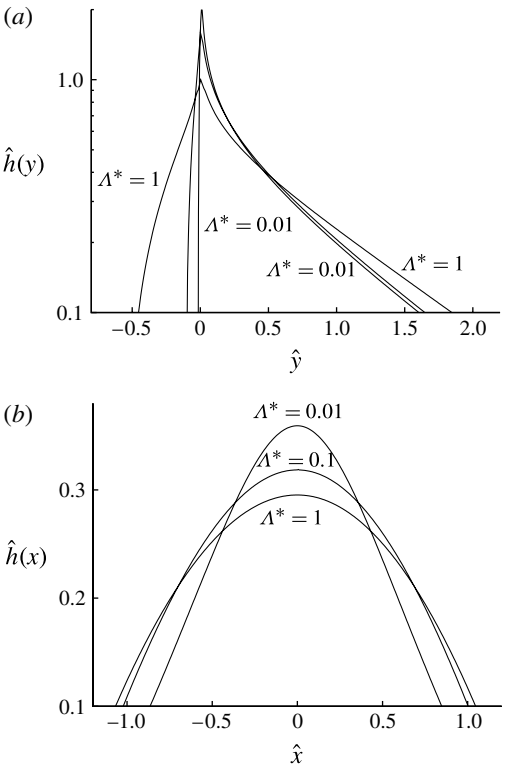


FIGURE 14. Numerical height of the plume (*a*) along-slope, at $\hat{x} = 0$ and (*b*) cross-slope, along the line of maximum spread for the contour of constant depth $\hat{h} = 0.1$, when $\Lambda^* = 1$, $\Lambda^* = 10^{-1}$ and $\Lambda^* = 10^{-2}$.

https://doi.org/10.1017/jfm.2013.199 Published online by Cambridge University Press

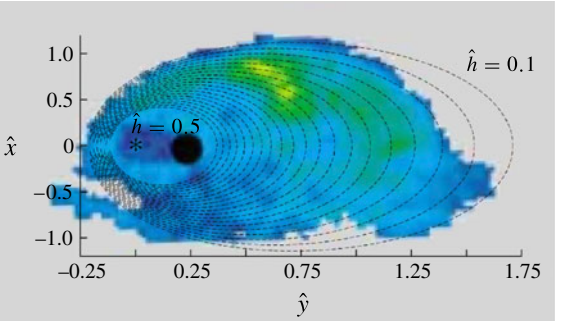


FIGURE 15. (Colour online) Comparison between the Horizon 1 plume observed in 2001 seismic survey at Sleipner and our numerical results for the steady state current when $\Lambda^* = 0.25$.

show some numerical predictions for the depth profiles of a plume, both along-slope (figure 14*a*) and cross-slope (figure 14*b*), for the cases $\Lambda^* = 0.01$, 0.1 and 1. It can be seen that the maximum depth is $\hat{h} \approx 1$ in all cases and thus the detection limit would correspond to the contour of constant depth $\hat{h}(\hat{x}, \hat{y}) = 0.1$. It should be noted that the cross-slope profiles in figure 14(b) are shown along the lines where the contour of constant depth $\hat{h} = 0.1$ reaches maximum width. It can also be seen from figure 14 that for this limit of $\hat{h} = 0.1$ the length of the plume is in all cases about $\mathscr{L} \approx 2L_D$, and the maximum width is also about $\mathscr{W} \approx 2W^*$. Thus we can immediately deduce that $L_D \approx 500$ m and $W^* \approx 275$ m. This means that $\Lambda^* = (W^*/L_D)^2 \approx 0.3$.

From our numerical results in § 6 (figure 10) it can be observed that, after scaling, the shape of the plume is not very sensitive to Λ^*; however the relative position of the source inside the plume varies significantly with Λ^*.

In figure 15 we show a comparison between the 2001 seismic image of the plume in Horizon 1 and our numerical solution for $\Lambda^* = 0.3$. It can be seen that the numerical solution matches fairly well the shape of the plume. Furthermore, our model predicts quite accurately the position of the source of CO_2 in the layer. As seen in figure 15, the numerical source at (0, 0), marked with an $*$, matches very well the position of the 'chimney' and this supports the assumption that CO_2 in Horizon 1 comes mainly from the 'chimney'.

If we can identify a value for H^* then we can estimate the total volume of CO_2 in the layer, given by $V = \phi L_D W^* H^*$. From (5.4) we know that $H^* = W^{*2}/L_D \tan\theta$, thus we only need θ to find an estimate of H^*. For a typical value $\theta = 1.5°$ we have $H^* \approx 4.5$ m and the limit depth of $\hat{h} = 0.1$ corresponds to $h = 0.45$ m, which is close to the reported detection limit of 0.5 m. The total volume estimate is $V = 618750\phi = 185625$ m^3, for a porosity value of $\phi = 0.3$ (Bickle *et al.* 2007). If we consider a density of $\rho = 607$ kg m^{-3} for the CO_2 in Horizon 1 (cf. Bickle *et al.* 2007), then our volume estimate corresponds to a total mass of 112.7 kt of CO_2. Bickle *et al.* (2007) give a value of 66 kt for layer 1, but their calculated volumes correspond only to the plume areas visible in the seismics. As mentioned before, for CO_2 thicknesses less than 0.5 m the seismic amplitudes were below the detection limit and consequently they report a 40 % underestimation of their calculated volumes, compared to the total mass of CO_2 injected in the formation. Our estimate is consistent with this rescaling of the Bickle *et al.* (2007) estimate.

https://doi.org/10.1017/jfm.2013.199 Published online by Cambridge University Press

In order to estimate the flux supplied to this layer, we should either use additional information about the flow, or adopt an estimate of the permeability in layer 1. The first approach is to observe the evolution of the plume before steady state, in order to identify the time needed to reach steady state. Although not shown explicitly here, we have found that for the contour of constant depth $\hat{h} = 1$ the time to reach steady state is $\sim 3T$–$4T$, where $T = \phi L_D/u$. No information prior to the 1999 seismic survey is available, but if we estimate that the plume in layer 1 has reached steady state by 1999, i.e. in 3 years, then it follows that $T \approx 0.75$–1 years. This would imply a flux of CO_2 in layer 1 of about $q \approx V/T$ 112–150 kt y^{-1}. The second approach consists of using the time scale $T = \phi L_D/u$, where the upslope speed $u = k\Delta\rho g \sin\theta/\mu$. With CO_2 viscosity in layer 1 being taken as $\mu = 4.56 \times 10^{-5}$ Pa s (cf. Bickle *et al.* 2007), it follows that the upslope speed is $u = 2.63k \times 10^6$ m s^{-1}. The permeability in layer 1 was measured to lie in the range $1.1 \leqslant k \leqslant 5 \times 10^{-12}$ m^2 (Bickle *et al.* 2007). Combining this information, the corresponding ranges for the time scale and the flux are $0.36 \leqslant T \leqslant 1.64$ years and $70 \leqslant q \leqslant 300$ kt y^{-1}. For an average value of $k = 2.5 \times 10^{-12}$ m^2, we have that $T = 0.723$ years and $q = 155$ kt y^{-1}. This means that Horizon 1 could receive about one-sixth of the total injected flux of CO_2, which may be a reasonable value if we consider that the chimney that feeds CO_2 goes up through all nine horizons.

8. Conclusions

The model presented herein, which builds from earlier models of the buoyant dispersal of fluid through an inclined permeable aquifer, with a fractured or weakly permeable upper boundary, predicts the fraction of the current and the shape of the region through which the buoyant fluid may drain to points higher into the formation. It also predicts the region in the original layer which may be flooded by the injected fluid.

First, we have developed the model for the case in which draining occurs through a localized fracture upslope of the source, while the remainder of the overlying cap rock is assumed to be impermeable. We have found that for a sloping boundary only a fraction of the flux drains through the fracture, in contrast a horizontal boundary (Pritchard 2007; Neufeld *et al.* 2009, 2011; Vella *et al.* 2011) in which case all the flux eventually drains through the boundary. We have calculated the fraction of the flow which drains and the fraction which continues beyond the fracture in the original formation. Our numerical solutions are consistent with simple analytical approximations.

We have then extended our analysis to account for multiple fractures in the upper boundary, and we have explored the limits when this model becomes equivalent to a model of draining through a low-permeability barrier. Our modelling identifies that for flow under a pervasively fractured or a weakly permeable seal rock, the injected fluid drains from the original layer within a finite zone from the source. Although our modelling is strictly relevant for miscible buoyant displacement flows, in the limit of small capillary force, the transition zone between a buoyant plume of CO_2 and the host fluid is relatively thin (cf. Golding *et al.* 2011), and so our results provide new insight into the migration of CO_2 as it spreads upslope. Following the injection phase, it is in this region that a fraction of the CO_2 may become trapped by capillary forces.

Although the model problem presented in this paper is simplified, the analysis identifies the scalings for the spatial evolution of a plume of CO_2 as it spreads from the injection point, and as illustrated in the applications above it points to the

https://doi.org/10.1017/jfm.2013.199 Published online by Cambridge University Press

balance between draining and the cross-slope dispersal of the plume. Such modelling allows scoping calculations of the dispersal of CO_2 in a potential site for a repository and provides insight into the relative importance of draining through seal rocks and leakage into fractures. There are several possible developments of the present modelling, including extension of the model to account for the effects of: (i) the displacement of the original reservoir fluid, as may be important in reservoirs of relatively small vertical extent (cf. Hesse *et al.* 2006; Gunn & Woods 2011); (ii) effects of the fractional flow and partial saturation of the pore space in the case of immiscible flow (Bear 1971; Pruess *et al.* 2003; Juanes *et al.* 2006); and (iii) effects of heterogeneities in the permeable rock, which can lead to dispersion and more complex migration of the plume (Bear 1971).

One of the important aspects of applying such models for prediction of the performance of a specific reservoir is the inclusion of uncertainties in the properties of the reservoir. Development of simplified analytical models, such as outlined in the present work, provide a rapid resource for exploration of the impact of such uncertainties on the model predictions. For example, if we envisage that the fracture spacing in a particular formation has a log-normal distribution, and that the fracture strength also follows a log-normal distribution, then the range of draining distances and hence the distal extent of a plume could be represented by the product of these distributions. In turn, this will have an impact on the prediction of the width of the current and the volume of CO_2 in the reservoir, in equilibrium, assuming a constant injection rate. Much more detailed analyses of such effects have been described in other contexts (Dagan & Neuman 1997) but there is probably considerable value in using these analytical results in a probabilistic fashion. In addition, in many cases, the formation rock tends to be highly heterogeneous, and this can lead to the development of preferential flow paths of the buoyant fluid through the porous medium.

Acknowledgements

We are grateful for funding from the BP Institute and the NDA in support of this work.

REFERENCES

BARENBLATT, G. I. 1996 *Scaling, Self-Similarity, and Intermediate Asymptotics*. Cambridge University Press.

BEAR, J. 1971 *An Introduction to Flow in Porous Media.* Wiley.

BENNION, B. & BACHU, S. 2006 The impact of interfacial tension and pore-size distribution/capillary pressure character on CO_2 relative permeability at reservoir conditions in CO_2 brine systems. SPE 99325. *SPE/DOE Symposium on Improved Oil Recovery.* Soc. of Petrol. Engrs.

BICKLE, M., CHADWICK, A., HUPPERT, H. E., HALLWORTH, M. & LYLE, S. 2007 Modelling carbon dioxide accumulation at Sleipner: implications for underground carbon storage. *Earth Planet. Sci. Lett.* **255**, 164–176.

BOAIT, F. C., WHITE, N. J., BICKLE, M. J., CHADWICK, R. A., NEUFELD, J. A. & HUPPERT, H. E. 2012 Spatial and temporal evolution of injected CO_2 at the Sleipner field, North Sea. *J. Geophys. Res.* **117**, B03309.

CHADWICK, R. A., ARTS, R. & EIKEN, O. 2005 4D seismic imaging of a CO_2 plume. In *Petroleum Geology: North-West Europe and Global Perspectives, Proceedings of the 6th Petroleum Geology Conference* (ed. A. G. Dore & B. A. Vining), pp. 1385–1399. Geological Society.

DAGAN, G. & NEUMAN, S. P. (Eds) 1997 *Subsurface Flow and Transport: A Stochastic Approach*. Cambridge University Press.

https://doi.org/10.1017/jfm.2013.199 Published online by Cambridge University Press

EVANS, J. P., FORSTER, C. B. & GODDARD, J. V. 1997 Permeability of fault-related rocks, and implications for hydraulic structure of fault zones. *J. Struct. Geol.* **19**, 1393–1404.

FARCAS, A. & WOODS, A. W. 2009 The effect of drainage on the capillary retention of CO_2 in a layered permeable rock. *J. Fluid Mech.* **618**, 349–359.

GOLDING, M. J., NEUFELD, J. A., HESSE, M. A. & HUPPERT, H. E. 2011 Two-phase gravity currents in porous media. *J. Fluid Mech.* **678**, 248–270.

GUNN, I. & WOODS, A. W. 2011 On the flow of buoyant fluid injected into a confined, inclined aquifer. *J. Fluid Mech.* **672**, 109–129.

HESSE, M. A., ORR, F. M. Jr & TCHELEPI, H. A. 2008 Gravity currents with residual trapping. *J. Fluid Mech.* **611**, 35–60.

HESSE, M. A., TCHELEPI, H. A., CANTWELL, B. J. & ORR, F. M. Jr 2007 Gravity currents in horizontal porous layers: transition from early to late self-similarity. *J. Fluid Mech.* **577**, 363–383.

HESSE, M. A., TCHELEPI, H. A. & ORR, F. M. Jr 2006 Scaling analysis of the migration of CO_2 in aquifers. SPE 102796. *SPE Annual Technicl Conference and Exhibition, San Antonio*. San Antonio.

HOMSY, G. M. 1987 Viscous fingering in porous media.. *Annu. Rev. Fluid Mech.* **19**, 271–311.

HUPPERT, H. E. & WOODS, A. W. 1995 Gravity-driven flows in porous layers. *J. Fluid Mech.* **292**, 55–69.

JUANES, R., SPITERI, E. J., ORR, F. M. Jr & BLUNT, M. J. 2006 Impact of relative permeability hysteresis on geological CO_2 storage. *Water Resour. Res.* **42**, W12418.

LISTER, J. R. 1992 Viscous flows down an inclined plane from point and line sources. *J. Fluid Mech.* **242**, 631–653.

DE LOUBENS, R. & RAMAKRISHNAN, T. 2011 Analysis and computation of gravity-induced migration in porous media. *J. Fluid Mech.* **675**, 60–86.

LOVOLL, G., MEHEUST, Y., MALOY, K. J., AKER, E. & SCHMITTBUHL, J. 2005 Competition of gravity, capillary and viscous forces, during drainage in a two-dimensional porous medium, a pore scale study. *Energy* **30**, 861–872.

LYLE, S., HUPPERT, H. E., HALLWORTH, M., BICKLE, M. & CHADWICK, A. 2005 Axisymmetric gravity currents in a porous medium. *J. Fluid Mech.* **543**, 293–302.

MITCHELL, V. & WOODS, A. W. 2006 Gravity driven flow in confined aquifers. *J. Fluid Mech.* **566**, 345–355.

NEUFELD, J. A. & HUPPERT, H. E. 2009 Modelling carbon dioxide sequestration in layered strata. *J. Fluid Mech.* **625**, 353–370.

NEUFELD, J. A., VELLA, D. & HUPPERT, H. E. 2009 The effect of a fissure on storage in a porous medium. *J. Fluid Mech.* **639**, 239–259.

NEUFELD, J. A., VELLA, D., HUPPERT, H. E. & LISTER, J. R. 2011 Leakage from gravity currents in a porous medium. Part 1. A localized sink. *J. Fluid Mech.* **666**, 391–413.

NORDBOTTEN, J. M. & CELIA, M. A. 2006 Similarity solutions for fluid injection into confined aquifers. *J. Fluid Mech.* **561**, 307–327.

OBI, E.-O. I. & BLUNT, M. J. 2006 Streamline-based simulation of carbon dioxide storage in a North Sea aquifer. *Water Resour. Res.* **42**, W03414.

PHILLIPS, O. M. 1991 *Flow and Reactions in Permeable Rocks*. Cambridge University Press.

PRITCHARD, D. 2007 Gravity currents over fractured substrates in a porous medium. *J. Fluid Mech.* **584**, 415–431.

PRITCHARD, D., HOGG, A. J. & WOODS, A. W. 2001 On the slow draining of a gravity current moving through a layered permeable medium. *J. Fluid Mech.* **444**, 23–47.

PRUESS, K., XU, T., APPS, J. A. & GARCIA, J. 2003 Numerical modelling of aquifer disposal of CO_2. *SPE J.* 49–60.

RIAZ, A., HESSE, M., TCHELEPI, H. & ORR, F. M. Jr 2006 Onset of convection in a gravitationally unstable diffusive boundary layer in porous media. *J. Fluid Mech.* **548**, 87–111.

VELLA, D. & HUPPERT, H. E. 2006 Gravity currents in a porous medium at an inclined plane. *J. Fluid Mech.* **555**, 353–362.

https://doi.org/10.1017/jfm.2013.199 Published online by Cambridge University Press

VELLA, D., NEUFELD, J. A., HUPPERT, H. E. & LISTER, J. R. 2011 Leakage from gravity currents in a porous medium. Part 2. A line sink. *J. Fluid Mech.* **666**, 414–427.

VERDON, J. & WOODS, A. W. 2007 Gravity-driven reacting flows in a confined porous aquifer. *J. Fluid Mech.* **588**, 29–41.

WOODS, A. W. 1999 Liquid and vapour flow in superheated rock. *Annu. Rev. Fluid Mech.* **31**, 171–199.

WOODS, A. W. & ESPIE, T. 2012 Controls on the dissolution of CO_2 plumes in structural traps in deep saline aquifers. *Geophys Res. Lett.* **39**, L08401.

WOODS, A. W. & FARCAS, A. 2009 Capillary entry pressure and the leakage of gravity currents through a sloping layered permeable rock. *J. Fluid Mech.* **618**, 361–379.

WOODS, A. W. & NORRIS, S. 2010 On the role of caprock and fracture zones in dispersing gas plumes in the subsurface. *Water Resour. Res.* **46**, W08522.

YORTSOS, Y. C. 1995 A theoretical analysis of vertical flow equilibrium. *Trans. Porous Med.* **18**, 107–129.

YORTSOS, Y. C. & HICKERNELL, F. J. 1989 Linear stability of immiscible displacement in porous media. *SIAM J. Appl. Maths* **49**, 730–748.

https://doi.org/10.1017/jfm.2013.199 Published online by Cambridge University Press